ADVANCED FUNCTIONAL MATERIALS
www.afm-journal.de



# Ultrasensitive Plasmonic Response of Bimetallic Au/Pd Nanostructures to Hydrogen

*Ruibin Jiang, Feng Qin, Qifeng Ruan, Jianfang Wang,* and Chongjun Jin**

**Hydrogen detection is crucial for the safety of all hydrogen-related applications. Compared to electrical hydrogen sensors, which usually suffer from possible electric sparks, optical hydrogen sensors offer advantages of remote and contact-free readout and therefore the avoidance of spark generation. Herein, bimetallic Au/Pd nanostructure monolayers that exhibit ultrasensitive plasmonic response to hydrogen are reported. Bimetallic Au/Pd nanostructures with continuous and discontinuous Pd shells are prepared. The plasmonic response to hydrogen is monitored by measuring the extinction spectra of the ensemble Au/Pd nanostructures deposited on glass slides. Introduction of hydrogen induces red plasmon shifts, which become larger for the nanostructures with thicker Pd shells. For the nanostructures with continuous Pd shell, the plasmon shift can reach 56 nm at the hydrogen volume concentration below the explosion limit. The plasmon resonance wavelength displays an excellent linear dependence on the hydrogen volume concentration below 1%. The detection limit in the experiments reaches 0.2%. The nanostructures with discontinuous Pd shell show smaller plasmon shifts than those with continuous Pd shell. The extinction measurements on the ensemble nanostructures supported on transparent substrates and the unprecedentedly large plasmon shifts and sensitivity make the results very promising for the development of practical optical hydrogen sensors.**

## 1. Introduction

The constantly decreasing fossil fuel reserves and climate changes caused probably by carbon dioxide emission have urged a necessity to develop alternative energy carriers. Hydrogen is one of the most promising clean and sustainable energy carriers for the replacement of current carbon-based energy sources.[1–3] It is being widely used in fuel cells, internal combustion engines, and household cooking and heating.[4,5] Moreover, hydrogen is also being used extensively in scientific research and industries, notably in glass and steel manufacturing as well as in the refining of petroleum products.[6] However, hydrogen is hazardous and easy to explode in air at volume concentrations ranging from 4% to 75% and with a low ignition energy of 0.02 mJ.[7] Therefore, effective hydrogen sensors that can quickly and sensitively respond to hydrogen are crucial for the safety of all hydrogen-related applications. Many efforts have been made on the design and fabrication of safe, reliable, cheap, and compact hydrogen sensors in recent years.[6–17]

Palladium serves as a major material for hydrogen sensing because of its thermodynamically suitable and fully reversible hydride formation properties under ambient conditions.[6,8–16] When Pd is exposed to hydrogen gas, hydrogen molecules dissociate and enter into the interstitial sites with octahedral or tetrahedral symmetry.[18] The insertion of hydrogen atoms induces mass and volume changes in the Pd host. Moreover, the electron associated with the hydrogen atom enters the *s*- and *d*-bands of palladium, which changes the density of electronic states at the Fermi level, causes shifts of the energy bands, and in turn alters the conductivity and dielectric properties.[18] These changes are the basis of hydrogen sensing using palladium. Because the changes in mass, volume, and dielectric property are very small and difficult to be measured, most Pd-based hydrogen sensors are realized by detecting the change in electrical conductivity.[6,14,15] On the other hand, optical hydrogen sensors relying on the change in dielectric property have a unique advantage that they can achieve remote contact-free readout. This advantage avoids electric sparks that can be generated in electrical hydrogen sensors and therefore increases the inherent safety.

Optical sensors based on localized surface plasmon resonance (LSPR) of noble metal nanostructures have attracted enormous interests from different areas, such as biology, medicine, chemistry, and environment.[19–21] A major type of LSPR-based optical sensors exploits the property that LSPR wavelengths and/or intensities are very sensitive to the dielectric changes caused by the adsorption of analyte species in the vicinity of noble metal nanostructures.[19–21] The insertion of hydrogen atoms into palladium results in the formation of palladium hydride, which is accompanied with the change of the dielectric function.[18] Therefore, integration of palladium with plasmonic

Dr. R. B. Jiang, F. Qin, Q. F. Ruan, Prof. J. F. Wang
Department of Physics
The Chinese University of Hong Kong
Shatin, Hong Kong SAR, China
E-mail: jfwang@phy.cuhk.edu.hk
Prof. C. J. Jin
State Key Laboratory of Optoelectronic Materials and Technologies
School of Physics and Engineering
Sun Yat-sen University
Guangzhou 510275, China
E-mail: jinchjun@mail.sysu.edu.cn

DOI: 10.1002/adfm.201402091

components can allow for plasmonic hydrogen sensing. Several types of bimetallic Au/Pd nanostructures, including Au/Pd heterodimers,[8,10] (Au core)/(Pd shell) nanocrystals,[12,22] and (Au nanosphere)/(Pd film) hybrid structures,[11] have been demonstrated for hydrogen sensing. The plasmon shifts and intensity changes of these nanostructures are relatively small when the hydrogen volume concentration is below 4%. For example, the maximal plasmon shift obtained on Au/Pd heterodimers is smaller than 10 nm,[8] and that produced by (Au core)/(Pd shell) nanocrystals is less than 25 nm.[12] Although plasmon shifts as large as 150 nm are obtained with aqueous (Au core)/(Pd shell) nanostructure solutions,[22] lithographically fabricated pure Pd nanodisks[23,24] and nanorings,[25] it should be pointed out that these plasmon shift measurements are performed with pure hydrogen, which is unrealistic for practical hydrogen sensing applications. In addition, very recently, (Au core)/(Pd shell) nanorod arrays have been fabricated by use of anodic alumina templates, and transmittance changes up to 30% have been obtained at the hydrogen volume concentration of 2%.[26]

In this work, we prepared two types of colloidal bimetallic Au/Pd nanostructures and examined their plasmonic response to hydrogen in nitrogen at low volume concentrations. One is Au nanorods encapsulated with continuous Pd shell (Au/c-Pd) and the other is Au nanorods decorated with discontinuous Pd shell (Au/d-Pd). The plasmonic response to hydrogen was monitored by recording the extinction spectra of the ensemble nanostructures that were deposited on transparent glass slides. The Au/c-Pd nanostructures exhibit a maximal red plasmon shift that is larger than the twice of the value obtained in previous related studies under the similar measurement conditions at the hydrogen volume concentration lower than the explosion limit. The Au/d-Pd nanostructures display smaller plasmon shifts than the Au/c-Pd ones. The plasmon shifts during the hydrogen exposure process were confirmed and understood with the assistance of electromagnetic simulations.

## 2. Results and Discussion

Because of their facile synthesis, good chemical stability, and synthetically tunable longitudinal plasmon wavelength, Au nanorods have been widely used in the control of optical processes,[27–29] photothermal conversion,[30,31] photocatalysis,[32–34] and solar cells.[35–37] In addition, the refractive index sensitivities of Au nanorods are generally larger than those of Au nanospheres.[38,39] We therefore chose Au nanorods as the core to prepare bimetallic Au/Pd nanostructures. **Figure 1** shows the transmission electron microscopy (TEM) images and extinction spectra of the uncoated Au nanorod sample and the bimetallic Au/Pd nanostructure samples that were prepared with cetyltrimethylammonium bromide (CTAB) surfactant as the stabilizing agent. The Au nanorod sample was synthesized with CTAB-capped Au nanoparticles as seeds. They are single-crystalline.[29,40] The average length and diameter measured from the TEM images (Figure 1a) of the Au nanorod sample are 96 ± 6 nm and 42 ± 3 nm, respectively. The extinction spectrum (Figure 1i) shows that the Au nanorod sample in aqueous solutions has a longitudinal plasmon resonance at 695 nm and a transverse one at 518 nm. Previous studies[40–43] indicate that bimetallic Au/Pd nanostructures prepared in the presence of CTAB surfactant possess continuous Pd shell. The continuous Pd shell is verified by TEM (Figure 1b–e) and high-angle annular dark-field scanning transmission electron microscopy (HAADF-STEM) imaging (Figure 1f) as well as elemental mapping (Figure 1g). Moreover, the electron diffraction patterns (Figure 1h) recorded on the individual Au/c-Pd nanostructures suggest that each entire nanostructure is single-crystalline. We produced Pd shell with different thicknesses by varying the amount of the Pd precursor. Four bimetallic Au/c-Pd nanocrystal samples with increasing shell thicknesses were made by adding 10 μL, 20 μL, 30 μL, and 40 μL of $H_2PdCl_4$ (0.01 M) into 1 mL of the aqueous Au nanorod solution. The

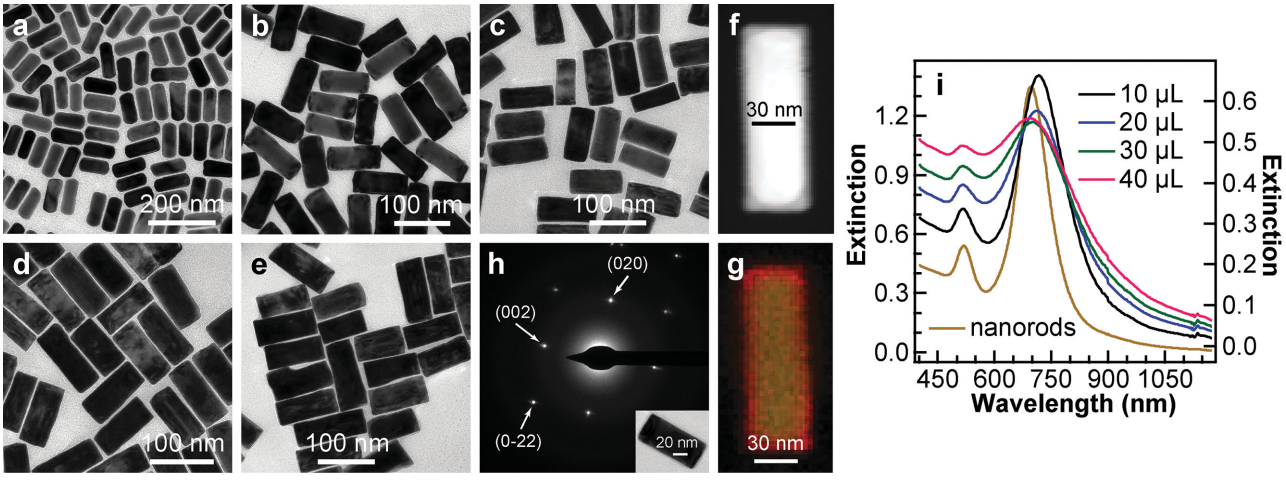


**Figure 1.** Au nanorods and bimetallic Au/c-Pd nanostructures. a) TEM image of the Au nanorod sample that was used as the core. b–e) TEM images of the Au/c-Pd nanostructure samples grown with 10 μL, 20 μL, 30 μL, and 40 μL of $H_2PdCl_4$ (0.01 M), respectively. The volume of the added ascorbic acid solution at 0.1 M is equal to a half of the $H_2PdCl_4$ solution for each nanostructure sample. Their average lengths/diameters are (96 ± 6)/(42 ± 3) nm, (97 ± 7)/(43 ± 4) nm, (99 ± 6)/(44 ± 3) nm, and (102 ± 9)/(47 ± 3) nm. f) HAADF-STEM image of a single nanostructure from the sample shown in (d). g) Merged elemental map of the same nanostructure as in (f). h) Electron-diffraction pattern of a [100]-oriented nanostructure (inset) from the sample shown in (d). i) Extinction spectra of the uncoated Au nanorod sample (left axis) and the four Au/c-Pd nanostructure samples (right axis). The extinction spectra of the uncoated Au nanorod sample and the Au/c-Pd nanostructure samples were measured at different particle concentrations.

effective Pd shell thicknesses of the four samples were calculated to be 0.73 nm, 1.65 nm, 2.55 nm, and 3.47 nm, respectively, according to the Pd mass concentration as well as the particle concentration and size of the Au nanorods. The Pd mass concentration was obtained from inductively coupled plasma optical emission spectrometry (ICP-OES). The particle concentration of the Au nanorods was calculated from the Au mass concentration obtained from ICP-OES and the average size measured from the TEM images according to the previously reported method.[44,45] Palladium is first deposited preferentially at the rounded ends of the Au nanorods, with the ends becoming flattened (Figure 1b). Therefore, when the amount of the palladium source is small, the average length and diameter of the nanostructure sample displays no observable changes because they are measured at the centers along the length and width axes. Although the flattening of the ends does not give rise to clear changes in length and diameter, it nevertheless results in a clear red shift in the longitudinal plasmon peak (Figure 1i) because of the increase of the effective aspect ratio of the nanocrystals.[46] When more Pd precursor is supplied, the nanostructures become cuboidal with relatively sharp edges and corners (Figure 1c–e). This growth behavior is consistent with our previous study on the overgrowth of palladium on single-crystalline Au nanorods.[40] We found that further Pd overgrowth causes blue shifts and broadening on the longitudinal plasmon resonance peak (Figure 1i). The evolution of the longitudinal plasmon with Pd overgrowth on Au nanorods has been ascertained systematically in our previous work.[41] The dielectric function of palladium has a negative real part and a relative large imaginary part. As the Pd shell is thickened, the metallic properties of palladium become more prominent with regard to the plasmon resonance of the bimetallic nanostructures. The negative real part of the dielectric function produces the blue shifts and the large imaginary part causes the broadening.

The ensemble Au/c-Pd nanostructures were deposited on glass slides and utilized to investigate their plasmonic responses to hydrogen. Our previous study has shown that the CTAB concentration in the nanocrystal solution as well as the hydrophilicity and cleanliness of glass slides are crucial for the formation of dense and uniformly distributed metal nanocrystals in large area.[47] Therefore, the CTAB concentration in the nanocrystal solution was controlled at ≈5 μM, and glass slides were washed and made hydrophilic. **Figure 2**a,b shows the low- and high-magnification scanning electron microscopy (SEM) images of the Au/c-Pd nanostructures deposited on glass slides. The bimetallic nanostructures are densely and relatively uniformly distributed. The majority of the nanostructures are spatially isolated. Slight aggregation probably results from dust particles, to which the nanostructures are preferentially attached. Because of their cuboidal shape, some nanostructures are oriented perpendicularly to the substrate surface and therefore look like squares with their edge lengths being the same as the transverse edge lengths of flatly lying ones (Figure 2b). Such perpendicular alignment of cuboidal nanocrystals is verified by the tilted SEM imaging of the Au/c-Pd nanostructures deposited on silicon substrates (Figure S1, Supporting Information) and has also been observed on TEM grids in our previous

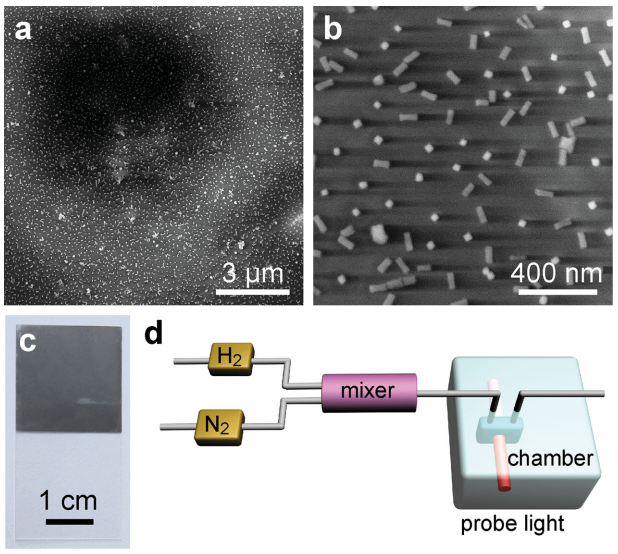


**Figure 2.** Bimetallic Au/c-Pd nanostructures deposited on glass slides. a,b) Low- and high-magnification SEM images of the deposited nanostructures. The nanostructure sample was prepared with 40 μL of $H_2PdCl_4$ (0.01 M). The square particles in the SEM images are nanostructures that are oriented with their length axis perpendicular to the glass substrate. c) Photograph of two square glass slides with the upper one deposited with the nanostructures and the lower one clean. d) Schematic of the setup for the hydrogen sensing measurements. The large box on the right represents the chamber of the spectrophotometer. The small box inside the large box represents the sample chamber.

experiments with (Au core)/(Ag shell) nanostructures.[40,48] Since the SEM images were taken directly on insulating glass slides, electron accumulation caused the appearance of dark and bright regions on the low-magnification SEM images and shadows on the high-magnification SEM images, respectively. The Au/c-Pd nanostructures supported on glass slides display grey black color (Figure 2c) owing to their large extinction in the entire visible region. Since the surfactant molecules on the Au/c-Pd nanostructures can possibly prevent hydrogen from interaction with palladium and thereby deteriorate the sensing performance, the deposited samples were treated with oxygen plasma to remove the surfactant molecules before the sensing measurements.

Figure 2d shows schematically the setup for the hydrogen sensing measurements. The volume concentration of hydrogen was controlled by two mass-flow controllers. Nitrogen was employed as a background gas. Before flowing into the measurement chamber, the two types of gases were effectively mixed in a mixing tube. After passing through the measurement chamber, the mixture gas was exhausted directly into air. As a result, the pressure in the measurement chamber was equal to the atmosphere pressure. In addition, our measurements were also carried out at room temperature. The measurement chamber had transparent windows at the front and back sides, which allowed for the passing of probing light. The extinction spectra of the deposited ensemble nanostructure samples were monitored on an ultraviolet/visible/near-infrared spectrophotometer for hydrogen detection.

We carried out the extinction measurements in three cycles for each Au/c-Pd nanocrystal sample to study their plasmonic

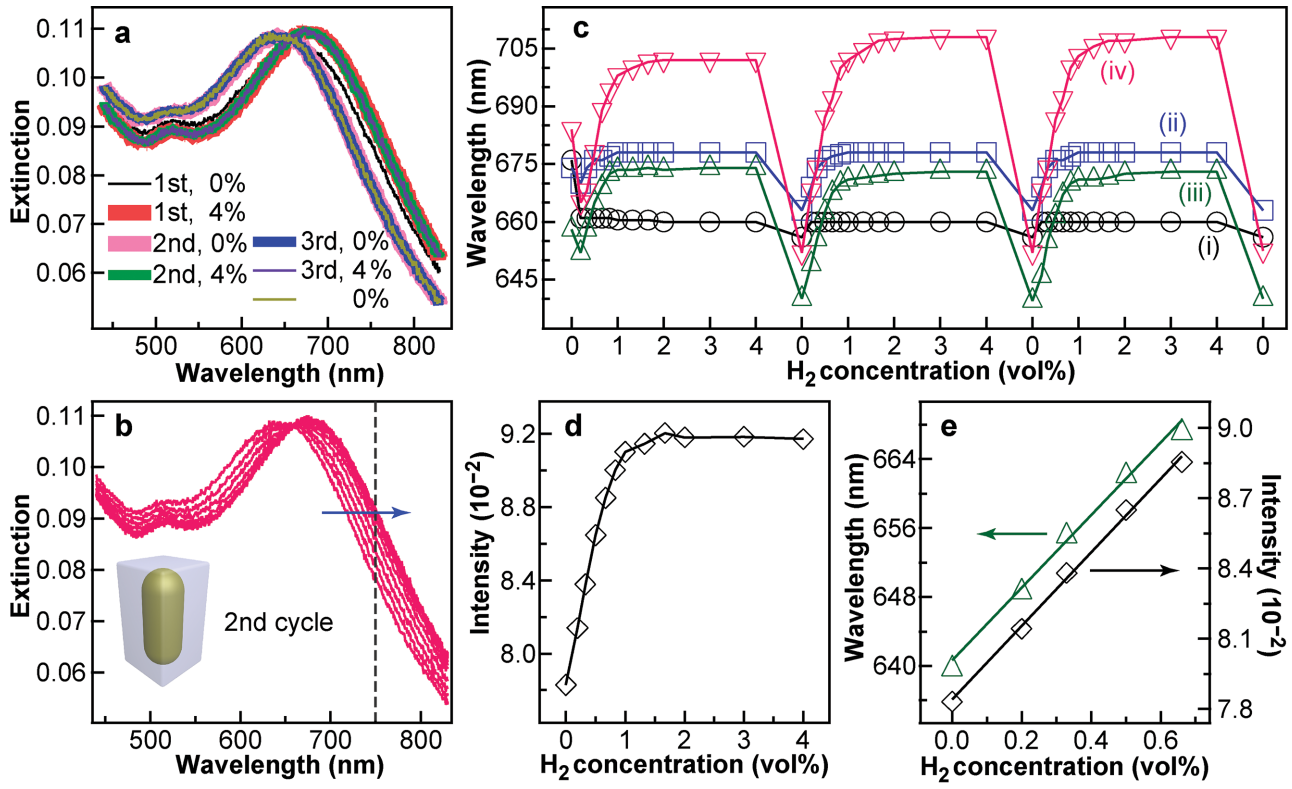


**Figure 3.** Plasmonic response of the bimetallic Au/c-Pd nanostructure samples to hydrogen. a) Extinction spectra of a nanostructure sample recorded at hydrogen volume concentrations of 0% and 4% in three cycles. The green-yellow spectrum was acquired when the hydrogen volume concentration was returned to 0% after the three cycles. b) Extinction spectra of a nanostructure sample taken in the second cycle for the hydrogen concentration varied from 0% to 4%. The arrow denotes the increase of the hydrogen concentration. The inset is the schematic of the nanostructure. c) Variations of the longitudinal plasmon wavelengths of the four nanostructure samples in three cycles as functions of the hydrogen concentration. (i), (ii), (iii), and (iv) are for the nanostructure samples prepared with 10 μL, 20 μL, 30 μL, and 40 μL of $H_2PdCl_4$ (0.01 M), respectively. d) Extinction intensity at 750 nm, as shown by the vertical black dashed line in (b), as a function of the hydrogen concentration. e) Linear dependences of the longitudinal plasmon wavelength (triangles, left axis) and extinction intensity (rhombuses, right axis) at 750 nm on the hydrogen concentration in the range from 0% to 0.66%. The symbols represent the experimental data, and the lines are fitted. The coefficients of determination for the wavelength and intensity fittings are 0.996 and 0.998, respectively. The nanostructure samples in (a,b,d,e) were made with 30 μL of $H_2PdCl_4$ (0.01 M).

response to hydrogen. **Figure 3**a displays the extinction spectra of the Au/c-Pd nanostructure sample grown with 30 μL of $H_2PdCl_4$ (0.01 M) at hydrogen volume concentrations of 0% and 4% in three cycles and after the hydrogen detection measurements. The plasmonic response to hydrogen exhibits good recyclability in the three cycles. The extinction spectra at 4% hydrogen overlap with one another in the three cycles. At 0% hydrogen, the extinction spectra in the second, third cycles and after the sensing measurements overlap with one another. The longitudinal plasmon peak wavelength measured at 0% hydrogen in the first cycle is longer than those measured in the later cycles. The longer plasmon wavelength measured in the first cycle is attributed to palladium oxide that is existent on the surface of the bimetallic nanostructures. Before being exposed to hydrogen, the nanostructure sample was treated with oxygen plasma, which caused the oxidation of palladium in the surface region. The presence of palladium oxide after oxygen plasma cleaning is confirmed by X-ray photoelectron spectroscopy (XPS), where the peaks arising from oxidized palladium[49] are observed (Figure S2, Supporting Information). After hydrogen introduction, palladium oxide is reduced back to palladium metal (Figure S2, Supporting Information). Because the real part of the dielectric function of Pd is negative[41] and that of palladium oxide is positive,[18,50] the oxidation of palladium in the surface region causes the longitudinal plasmon wavelength of the nanostructure sample after oxygen plasma cleaning to be longer than that of the reduced nanostructure sample at 0% hydrogen.

In each cycle, the hydrogen concentration was gradually increased to its explosion limit. In order to find out the response time, we measured the extinction spectra as a function of time at each hydrogen volume concentration. The extinction spectrum recorded immediately after the change of the hydrogen concentration was found to be the same as that obtained 10 min later at the same hydrogen concentration. The measurement of each spectrum took 1.5 min. This result suggests that the response time of our nanostructure samples is less than 1.5 min. As an example, Figure 3b shows the extinction spectra measured in the second cycle for the Au/c-Pd nanostructure sample prepared with 30 μL of the Pd precursor. The longitudinal plasmon wavelength of the sample red-shifts gradually with the increase of the hydrogen concentration when it is lower than ≈2% (Figure 3c). When the hydrogen concentration is higher than ≈2%, its further increase does not generate

observable plasmon shifts. The red plasmon shifts at hydrogen concentrations lower than ≈2% are caused by the formation of palladium hydride, because it has a larger refractive index than palladium.[18] No further plasmon shifts at hydrogen concentrations higher than ≈2% can be understood by the saturation of hydrogen atoms in palladium. Since the thickness of the Pd shell is only a few nanometers, the amount of hydrogen atoms in palladium is easy to reach saturation. The variation of the extinction spectra in the third cycle (Figure S3, Supporting Information) is very similar to that in the second cycle. In the beginning of the first cycle (Figure S3, Supporting Information), exposure to hydrogen gas leads to a blue shift of the longitudinal plasmon peak. Further increase of the hydrogen concentration causes red shifts. As discussed above, this plasmon shift behavior can be understood by the reduction of surface palladium oxide and the transformation of palladium into palladium hydride.

The plasmonic response of other three Au/c-Pd nanostructure samples to hydrogen is also systematically studied (Figure S4–S6, Supporting Information). The overall extinction variation trends are very similar to that of the nanostructure sample grown with 30 μL of the palladium source. For each sample, the extinction spectra acquired at 4% hydrogen in the three cycles overlap with one another. In the second and third cycles as well as after the measurements, the longitudinal plasmon peak at 0% hydrogen is located at the same wavelength, which is shorter than that measured in the first cycle at 0% hydrogen. In the first cycle, the longitudinal plasmon peak first blue-shifts and then red-shifts with increasing hydrogen concentrations. In the second and third cycles, as the hydrogen concentration is increased, the plasmon peak first shows red shifts and then remains nearly unchanged.

The longitudinal plasmon wavelengths obtained in the three measurement cycles for the four nanostructure samples are plotted as functions of the hydrogen volume concentration in Figure 3c. The four nanostructure samples show similar plasmonic response trends to hydrogen. In the first cycle, the longitudinal plasmon resonances of the four samples are blue-shifted in the beginning. Further increase of the hydrogen concentration does not change the plasmon wavelength of the Au/c-Pd nanostructure sample grown with 10 μL of the palladium source, but causes red shifts of the longitudinal plasmon peaks of the other three samples. In the second and third cycles, the plasmon peaks of the four samples exhibit red shifts first and then remain at nearly constant wavelengths when the hydrogen volume concentration is higher than certain values, which increase as the Pd shell gets thicker. The maximal plasmon shifts from 0% to 4% measured in the second and third cycles increase as the Pd shell becomes thicker. They are 4 nm, 15 nm, 34 nm, and 56 nm for the Au/c-Pd nanostructure samples made with 10 μL, 20 μL, 30 μL, and 40 μL of the palladium precursor, respectively. The largest plasmon shift, 56 nm, is more than twice the largest value reported up to date at 4% hydrogen under the similar measurement conditions.[12] In addition, we performed a five-cycle sensing measurement with the Au/c-Pd nanostructure sample made with 30 μL of the palladium precursor. The plasmonic responses to varying hydrogen volume concentrations in the second to fifth cycle appear nearly identical. The good repeatability indicates that the remarkable sensing performance of our Au/c-Pd nanostructure samples is well preserved after each cycle. This is different from the previous related studies, where the plasmon resonance cannot recover back to its initial wavelength.[8] This difference is probably due to the thin Pd shells on our nanostructures. The thin Pd shells can facilitate the release of hydrogen.

Besides the plasmon shifts, the extinction intensity at a given wavelength also changes with the hydrogen volume concentration. Figure 3d displays the extinction intensity change at 750 nm in the second cycle for the Au/c-Pd nanostructure sample grown with 30 μL of $H_2PdCl_4$. The intensity increases with the hydrogen concentration first and then remains at a steady value. The relative intensity change reaches 17%. Both the plasmon resonance wavelength and extinction intensity show very good linear dependences on the hydrogen concentration at low values (Figure 3e). Moreover, Figure 3e reveals that our bimetallic nanostructures can give a clear plasmon shift and intensity change even at hydrogen volume concentrations as low as 0.2%. By taking into account the linear dependence at low hydrogen concentrations and if we assume that plasmon shifts at 1 nm can be resolved instrumentally, the detection limit of our Au/c-Pd nanostructures for hydrogen can be potentially as low as 0.024%. The high sensitivity of our Au/c-Pd nanostructures can be understood as follows. Palladium forms a continuous shell around Au nanorods. The transformation from palladium into palladium hydride changes the entire surrounding medium around Au nanorods and therefore alters the plasmon resonance notably. Because the local electric field enhancement decays approximately exponentially away from the surface of Au nanorods (Figure S7, Supporting Information), the LSPR sensitivity falls off quickly with the distance away from the surface of plasmonic metal nanostructures.[19,51] In our nanostructures, the intimate integration of palladium with Au nanorods makes palladium located in the region with the largest electric field enhancement. The change in the dielectric function of the shell can therefore give rise to a larger LSPR sensitivity in comparison with other nanostructures, such as Au/Pd heterodimers.[8] In addition, within the range comparable to the field enhancement decay length, the plasmon shift induced by a dielectric shell coated on plasmonic metal nanostructures increases with the shell thickness.[52] This explains our observation that the maximal plasmon shift between 0% and 4% hydrogen increases with the Pd shell thickness.

Au/d-Pd nanostructures display small plasmon damping and good photocatalytic properties.[33,41] We therefore tried to examine whether they are plasmonically more sensitive to hydrogen than the Au/c-Pd nanostructures. Au/d-Pd nanostructure samples were prepared under the same conditions except that the surfactant was changed from CTAB to cetyltrimethylammonium chloride (CTAC). **Figure 4**a–d show the TEM images of the Au/d-Pd nanostructure samples grown with 10 μL, 20 μL, 30 μL, and 40 μL of the palladium precursor, respectively. The discontinuous Pd shell is composed of small Pd nanoparticles, as revealed by TEM imaging, HAADF-STEM imaging, and elemental mapping (Figure 4a–f). Our previous studies have shown that the small Pd nanoparticles are epitaxially overgrown on Au nanocrystals with their sizes being 4–5 nm in diameter.[33,41] As the volume of the palladium source is increased, the Pd nanoparticles are packed more densely on

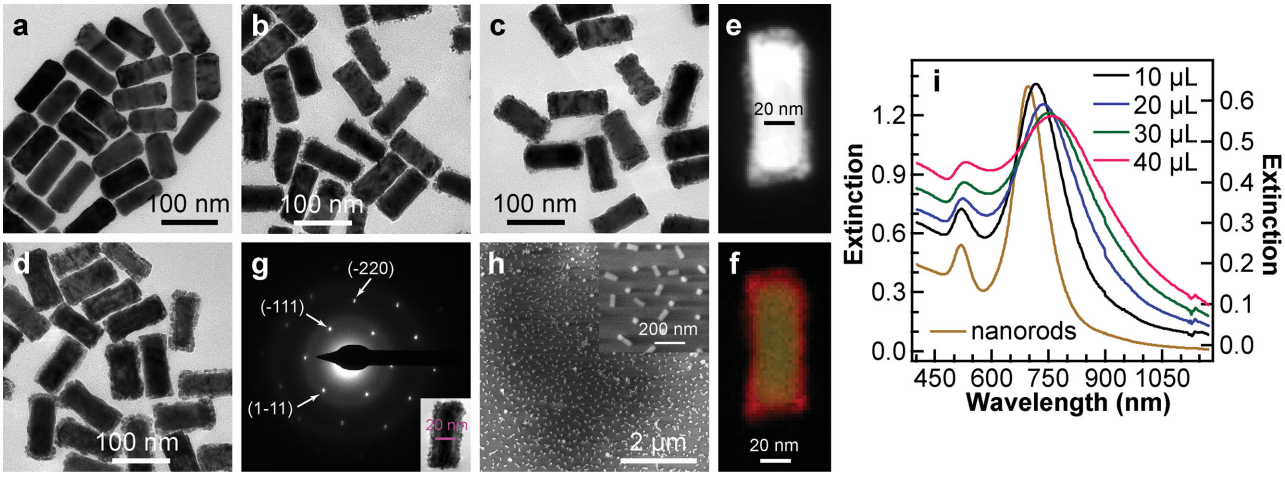


**Figure 4.** Bimetallic Au/d-Pd nanostructures. a–d) TEM images of the nanostructure samples grown with 10 μL, 20 μL, 30 μL, and 40 μL of $H_2PdCl_4$ (0.01 M), respectively. The volume of the added ascorbic acid solution at 0.1 M was equal to a half of that of $H_2PdCl_4$ for each sample. e) HAADF-STEM image of a nanostructure from the sample in (d). f) Merged elemental map of the nanostructure shown in (e). g) Electron-diffraction pattern of a [110]-oriented nanostructure (inset) from the sample in (d). h) SEM image of the nanostructure sample that is shown in (d) and deposited on a glass slide. The inset is a high-magnification SEM image. Nanostructures oriented perpendicular to the substrate surface appear as smaller squares. i) Extinction spectra of the uncoated Au nanorod sample (left axis) and the four nanostructure samples (right axis). The extinction spectra of the Au nanorod sample and the nanostructure samples were measured at different particle concentrations.

the Au nanorod surface. We again used the effective shell thickness to describe the amount of Pd on the Au/d-Pd nanostructures even though the shell was composed of discrete Pd nanoparticles. The effective shell thicknesses were calculated from the Pd mass concentration as well as the particle concentration and size of the Au nanorods to be 0.78 nm, 1.71 nm, 2.58 nm, and 3.51 nm for the four samples, respectively. Because the Pd shell is composed of many Pd nanoparticles orientated in different directions, the Au/d-Pd nanostructures are polycrystalline.[33] The polycrystallinity cannot be revealed by selected-area electron diffraction patterns recorded on the single Au/d-Pd nanostructures (Figure 4g), because the diffraction signal from the small Pd nanoparticles is too weak to be detected. Figure 4h shows the SEM images of the Au/d-Pd nanostructure sample that was grown with 40 μL of $H_2PdCl_4$ and deposited on glass slides. The deposited nanostructures are densely and uniformly distributed on glass slides. Aggregation is slight. Some nanostructures are oriented perpendicular to the substrate surface because of their flat ends. The extinction spectra of the uncoated Au nanorod sample and the obtained Au/d-Pd nanostructure samples are shown in Figure 4i. As more palladium source is supplied, the longitudinal plasmon resonance peak shows gradual red shifts. We have shown previously that the real part of the dielectric function of the discontinuous Pd shell is positive when the Pd volume fraction in the shell is smaller than the plasmonic percolation threshold.[41] The positive real part of the dielectric function causes red shifts in the longitudinal plasmon resonance peak. In addition, the overgrowth of Pd nanoparticles broadens the plasmon peak due to the large imaginary part of the dielectric function of palladium.

The plasmonic response of the Au/d-Pd nanostructure samples to different volume concentrations of hydrogen is also monitored in three cycles (**Figure 5**a,b together with Figure S8–S11, Supporting Information). The extinction spectra for each nanostructure sample overlap with one another at 4% hydrogen in all of the three cycles. At 0% hydrogen, except in the first cycle, the longitudinal plasmon wavelengths obtained in the second and third cycles and after the measurements are the same. The peculiarity in the first cycle is caused by surface palladium oxide. These observations suggest that the Au/d-Pd nanostructure samples are also relatively stable after being exposed to hydrogen repeatedly.

In the first cycle, the initial exposure to hydrogen gas leads to prominent blue shifts of the longitudinal plasmon peak, owing to the reduction of surface palladium oxide into palladium by hydrogen (Figure 5c). Further increase of the hydrogen volume concentration induces red shifts of the longitudinal plasmon peak for the Au/d-Pd nanostructure sample grown with 40 μL of $H_2PdCl_4$, but does not cause clear plasmon shifts for the other three samples. In the second and third cycles, as the hydrogen concentration is gradually increased, the longitudinal plasmon peaks of all of the four samples gradually move in the longer-wavelength direction first and finally reach constant wavelengths. The variations of the longitudinal plasmon wavelengths of the four samples as functions of the hydrogen concentration in the three cycles, as plotted in Figure 5c, indicate that the Au/d-Pd nanostructure samples possess good stability after interaction with hydrogen molecules. The plasmonic response to hydrogen becomes more sensitive with the increase in the amount of Pd nanoparticles on Au nanorods. The maximal plasmon shift from 0% to 4% hydrogen increases from 2 nm to 17 nm when the amount of the palladium precursor used in the preparations is increased from 10 μL to 40 μL. Compared with the Au/c-Pd nanostructures, the Au/d-Pd nanostructures obtained with the same palladium source give smaller plasmon shifts. This is because only a fraction of the surface region surrounding Au nanorods is changed from palladium to palladium hydride for the Au/d-Pd nanostructures, whereas the entire surface region surrounding Au nanorods is varied from palladium to palladium hydride for the Au/c-Pd

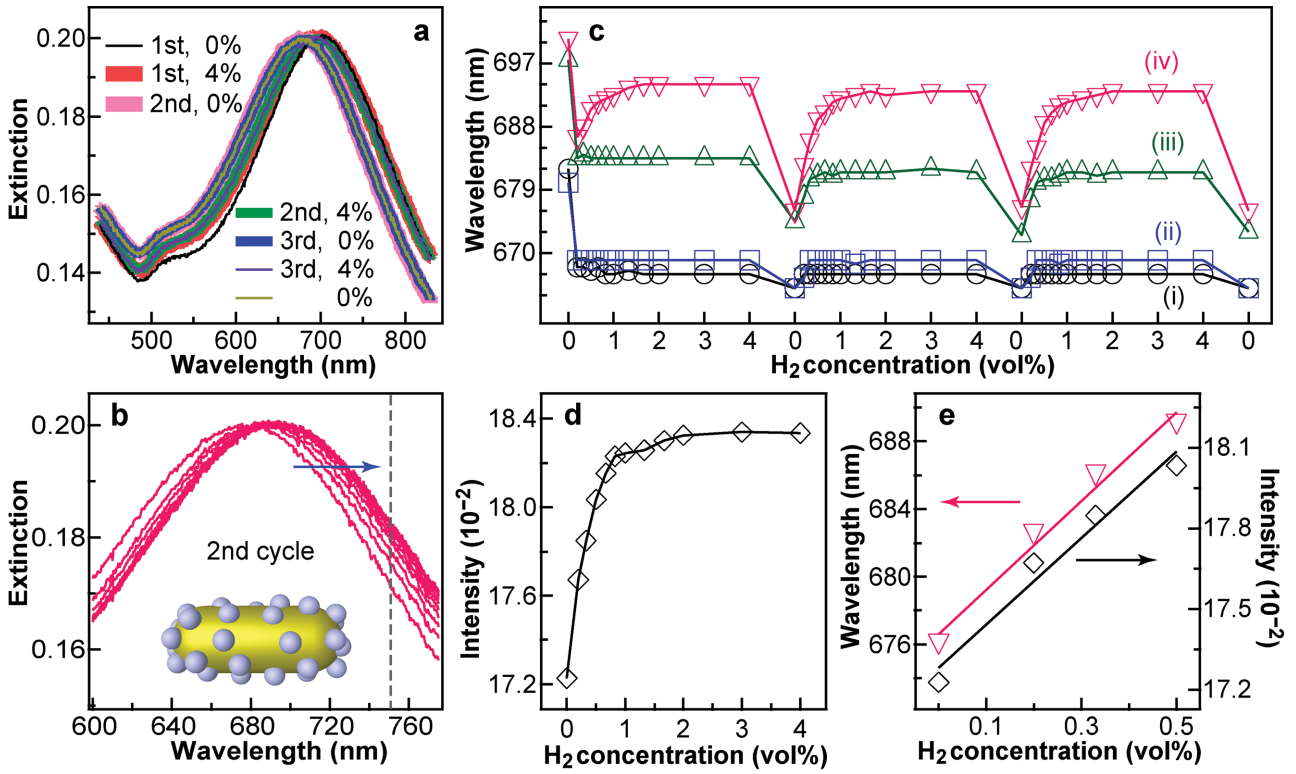


**Figure 5.** Plasmonic response of the bimetallic Au/d-Pd nanostructure samples to hydrogen. a) Extinction spectra of a nanostructure sample recorded at hydrogen volume concentrations of 0% and 4% in three cycles. The green-yellow spectrum was acquired when the hydrogen volume concentration was returned to 0% after the three cycles. b) Extinction spectra of a nanostructure sample taken in the second cycle for the hydrogen concentration varied from 0% to 4%. The arrow denotes the increase of the hydrogen concentration. The inset is the schematic of the nanostructure. c) Variations of the longitudinal plasmon wavelengths of the four nanostructure samples in three cycles as functions of the hydrogen concentration. (i), (ii), (iii), and (iv) are for the nanostructure samples prepared with 10 μL, 20 μL, 30 μL, and 40 μL of $H_2PdCl_4$ (0.01 M), respectively. d) Extinction intensity at 750 nm, as indicated by the vertical grey dashed line in (b), as a function of the hydrogen concentration. e) Linear dependences of the longitudinal plasmon wavelength (triangles, left axis) and extinction intensity (rhombuses, right axis) at 750 nm on the hydrogen concentration in the range from 0% to 0.5%. The symbols represent the experimental data, and the lines are fitted. The coefficients of determination for the wavelength and intensity fittings are 0.990 and 0.983, respectively. The nanostructure samples in (a,b,d,e) were made with 40 μL of $H_2PdCl_4$.

nanostructures. In addition, we found that the longitudinal plasmon wavelengths of all of the four Au/d-Pd nanostructure samples before being exposed to hydrogen gas are longer than the corresponding ones after being exposed to 4% hydrogen (Figure 5c). In contrast, the longitudinal plasmon wavelengths of the Au/c-Pd nanostructures with a thicker Pd shell at 4% hydrogen are longer than the corresponding values before exposure to hydrogen gas (Figure 3c). This difference might result from two reasons. One is that the amount of palladium that is oxidized during oxygen plasma treatment is larger for the Au/d-Pd nanostructures than for the Au/c-Pd nanostructures, owing to the larger surface area of the former. The other is that the plasmon shift caused by exposure to hydrogen gas is smaller for the Au/d-Pd nanostructures than for the Au/c-Pd nanostructures. Similar to the case of the Au/c-Pd nanostructures, the extinction intensity at a given wavelength for the Au/d-Pd nanostructures varies with the hydrogen concentration (Figure 5d). At low hydrogen concentrations, the dependences of both the wavelength and extinction intensity on the hydrogen concentration are highly linear (Figure 5e).

We further performed finite-difference time-domain (FDTD) simulations for the two types of bimetallic Au/Pd nanostructures to qualitatively elucidate the underlying reason for the plasmonic response to hydrogen. Previous studies have shown that glass substrates do not induce the occurrence of new plasmonic behaviors for relatively small supported Au nanocrystals[53,54] and that FDTD simulations in a homogeneous medium can effectively reproduce the plasmonic properties of Au nanocrystals supported on glass substrates.[55] Our simulations were therefore carried out in a homogeneous medium in order to clearly unravel the involved plasmonic properties. **Figure 6**a shows the simulation results for the Au/c-Pd nanostructure. The nanostructure of the Au nanorod coated with pure, continuous Pd shell has the shortest longitudinal plasmon wavelength. When the entire Pd shell is transformed into palladium hydride, the longitudinal plasmon resonance peak is red-shifted. The nanostructure with surface palladium oxide has its plasmon peak in between those of the nanostructures with pure Pd shell and with palladium hydride shell. The relative magnitudes of the longitudinal plasmon wavelengths for the three types of Pd-containing shells are consistent with the experimental ones (Figure 3a). The electric field intensity enhancement in the $PdH_x$ shell is clearly larger than that in the Pd shell (Figure 6b,c). This change in the field intensity enhancement

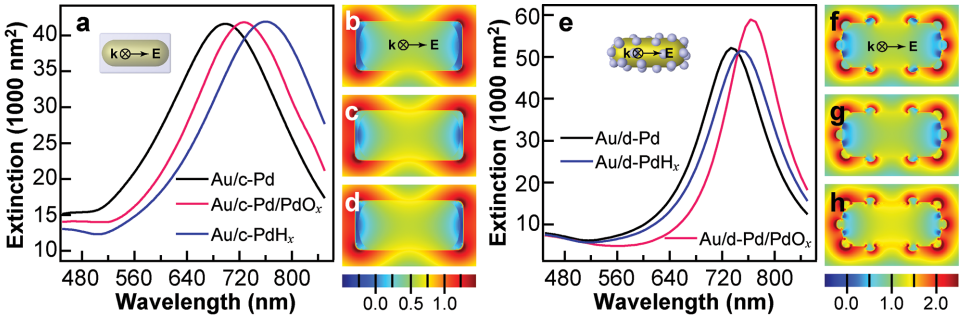


**Figure 6.** FDTD simulation results of the bimetallic and related nanostructures. a) Extinction spectra of the Au/c-Pd nanostructure under the different situations. b–d) Logarithmic electric field intensity enhancement contours of the Au/c-Pd, Au/c-PdH$_x$, and Au/c-Pd/PdO$_x$ nanostructures. e) Extinction spectra of the Au/d-Pd nanostructure under the different situations. f–h) Logarithmic electric field intensity enhancement contours of the Au/d-Pd, Au/d-PdH$_x$, and Au/d-Pd/PdO$_x$ nanostructures. The insets in (a,e) show the schematics of the nanostructures, the directions of the excitation wave propagation and electric field. The contours in (b–d,f–h) are drawn on the cross section that is perpendicular to the excitation wavevector and passes through the center of the nanostructure. They are simulated at the longitudinal plasmon wavelengths.

suggests that the shell is turned from metal to dielectric, which results in a red shift of the longitudinal plasmon of the bimetallic nanostructure. The field intensity enhancements of the Au/c-Pd and Au/c-Pd/PdO$_x$ nanostructures are similar except that the field enhancement in the PdO$_x$ shell is larger (Figure 6d).

The simulated extinction spectra for the Au/d-Pd nanostructures are plotted in Figure 6e. The nanostructure with surface palladium oxide has the longest plasmon resonance wavelength. After palladium oxide is reduced into palladium, the plasmon resonance is blue-shifted. When Pd nanoparticles are completely transformed into palladium hydride, the plasmon resonance wavelength of the nanostructure is in between those of the Au/d-Pd and Au/d-Pd/PdO$_x$ nanostructures. Moreover, the extinction cross-section of the Au/d-Pd/PdO$_x$ nanostructure is larger than those of the other two nanostructures. These results are in good agreement with the experimental ones (Figure 5a). The electric field intensity enhancements suggest that the enhancements in both PdH$_x$ and Pd/PdO$_x$ shells are larger than that in the Pd nanoparticles, and that the Au/d-Pd/PdO$_x$ nanostructure gives the largest field enhancement in the Au nanorod (Figure 6f–h). The change in the electric field intensity enhancement reflects the variation of the longitudinal plasmon resonance.

## 3. Conclusions

We have prepared two types of bimetallic Au/Pd nanostructures and studied their plasmonic response to hydrogen. The nanostructures with continuous and discontinuous Pd shell are synthesized in the presence of CTAB and CTAC surfactants, respectively. Their plasmonic response to hydrogen is measured on the ensemble Au/Pd nanostructures deposited on transparent glass slides. In the first measurement cycle, the longitudinal plasmon peaks of the two types of bimetallic nanostructures first blue-shift and then red-shift with increasing hydrogen concentrations. In the following cycles, the increase in the hydrogen concentration gives rise to red shifts in the plasmon peaks of the two types of bimetallic nanostructures. The plasmonic response sensitivy of both Au/c-Pd and Au/d-Pd nanostructures improves with the increase in the Pd shell thickness and the amount of overgrown Pd nanoparticles, respectively. At low hydrogen concentrations, both the plasmon wavelength and extinction intensity at a given wavelength show very good linearity with the hydrogen concentration. For the Au/c-Pd nanostructures, the plasmon shifts reach 56 nm when the hydrogen concentration is lower than the explosion limit. The detection limit of the hydrogen concentration in our experiments can reach 0.2%. Because only a portion of the adjacent surrounding medium is changed after exposure to hydrogen gas, the Au/d-Pd nanostructures exhibit smaller plasmon shifts than the Au/c-Pd nanostructures. The plasmonic sensing performance of the bimetallic nanostructures has been understood with the assistance of numerical electrodynamic simulations. The large plasmon shifts and easy measurements make our detection method very promising in developing plasmonic hydrogen sensors for practical applications.

## 4. Experimental Section

*Growth of the Bimetallic Au/Pd Nanostructures*: All of the bimetallic nanostructure samples were prepared in aqueous solutions using a seed-mediated growth method. The Au nanorod samples, obtained from NanoSeedz, were dispersed in CTAB (0.1 M). The Au/Pd nanostructures were prepared according to a reported procedure with slight modifications.[40,41] For the preparation of the Au/c-Pd nanostructures, four aliquots (1 mL) of the Au nanorod solution were centrifuged and redispersed into CTAB (0.025 M) at the same volume. 10 μL, 20 μL, 30 μL, and 40 μL of $H_2PdCl_4$ (0.01 M) were subsequently added into the four aliquots, respectively, followed by the addition of ascorbic acid (0.1 M). The volume of the ascorbic acid solution was a half of the $H_2PdCl_4$ solution for each aliquot. The resultant solutions were kept undisturbed for 5 h. For the preparation of the Au/d-Pd nanostructures, the procedure was the same as that for the preparation of the Au/c-Pd nanostructures except that the surfactant was changed from CTAB to CTAC (0.025 M).

*Deposition of the Bimetallic Nanostructures*: The cover glass slides purchased from Ted Pella, Inc. were washed with ethanol in ultrasonic bath (Blackstone-NEY Ultrasonics, 28H) for 20 min. Subsequently, the slides were blown dry with nitrogen gas. The obtained slides were then immersed into the bimetallic Au/Pd nanostructure solutions with the CTAB concentration adjusted to be ≈5 μM. After being kept overnight, the slides were taken and blown dry gently. Since the surface of the

CTAB-capped Au/Pd nanostructures is positively charged and the surface of the washed glass slides is negatively charged, the nanostructures can form a dense monolayer on the glass surface. The slides deposited with the Au/Pd nanostructures were treated with oxygen plasma (18 W, Harrick Scientific, PDC-32G) for 5 min to remove the capping CTAB molecules before the hydrogen sensing measurements.

*Characterization and Measurements of the Plasmonic Response to Hydrogen*: SEM imaging was performed on an FEI Quanta 400 FEG microscope. TEM imaging and electron-diffraction measurements were carried out on an FEI Tecnai Spirit microscope operating at 120 kV. HAADF-STEM imaging and energy-dispersive X-ray elemental mapping were performed on an FEI Tecnai F20 microscope equipped with an Oxford energy-dispersive X-ray analysis system. XPS characterization was carried out on a Thermo-VG Scientific ESCALAB 250 X-ray photoelectron spectrometer with Al K$\alpha$ radiation ($h\nu$ = 1486.6 eV). The ICP-OES measurements were performed on a PerkinElmer Optima 4300DV system. The nanostructure samples were centrifuged to remove the un-reacted Pd precursor. The precipitates were dissolved by a small amount of aqua regia and the obtained solutions were then diluted to a controlled volume for the ICP-OES measurements. The Pd and Au mass concentrations in the solutions were determined according to the pre-calibrated linear relationships between the emission intensity and the atomic mass concentration (Figure S12, Supporting Information). Extinction spectra were taken on a Hitachi U-3501 ultraviolet/visible/near-infrared spectrophotometer. The plasmonic response to hydrogen was monitored by measuring the extinction spectra of the ensemble nanostructure samples on the Hitachi spectrophotometer. The flow rates of nitrogen and hydrogen gas were controlled by two mass flow controllers (Horiba Metron, S48 32/HMT). The total gas flow rate was kept at 3 sccm (standard cubic centimeters per minute).

*FDTD Simulations*: All simulations were performed using FDTD Solutions 7.5 (Lumerical Solutions). During the simulations, an electromagnetic pulse from 400 nm to 850 nm was launched into a box containing the target nanostructure. The nanostructure and its surrounding medium were divided into meshes of 0.25 nm in size. The refractive index of the surrounding medium was set to be 1. The excitation electric field was polarized along the length axis. The Au nanorod core was modeled as a cylinder capped with a hemi-ellipsoid at each end. The diameter and length of the Au nanorod core were set to be the experimental values of 42 nm and 96 nm, respectively. The radii of the capping hemi-ellipsoid were 10 nm and 21 nm along the length and width axes of the nanorod core, respectively. The entire Au/c-Pd nanocrystal was modeled as a cuboid with slightly rounded corners and edges, with the radii of both the rounding sphere and cylinder set to be 6 nm. The total length and width of the Au/c-Pd nanostructure were 102 nm and 47 nm, respectively, which were the average values of the Au/c-Pd nanostructures grown with 40 μL of $H_2PdCl_4$. The Au/d-Pd nanostructure was modeled by attaching hemispherical Pd nanoparticles of 5 nm in diameter onto the Au nanorod, with the bottom of each Pd nanoparticle slightly deformed to be in tight contact with the Au nanorod surface. After exposure to hydrogen gas, we assumed that the entire Pd shell or all Pd nanoparticles were completely transformed into palladium hydride. For the nanostructure with surface palladium oxide, palladium in the 1-nm-thick surface region of the Pd shell or the Pd nanoparticles was set to be palladium oxide. The dielectric functions of gold, palladium, palladium hydride, and palladium oxide were taken from previously reported values.[18,50,56]

## Supporting Information

Supporting Information is available from the Wiley Online Library or from the author. It includes the XPS data of the Au/c-Pd nanostructure sample prepared with 30 μL of $H_2PdCl_4$ under different situations, the extinction spectra of the bimetallic Au/Pd nanostructure samples recorded in different cycles as functions of the hydrogen volume concentration, and the electric field intensity enhancement contours and decay profiles of the uncoated Au nanorod.

## Acknowledgements

This work was supported by Hong Kong Research Grants Council (SRFDP/RGC ERG, Ref. No. M-CUHK410/12, Project Code 2900701 and CRF, Ref. No. CUHK1/CRF/12G, Project Code 2390064). The FDTD simulations were conducted in the High Performance Cluster Computing Centre, Hong Kong Baptist University, which is supported by Hong Kong RGC and Hong Kong Baptist University. The authors are particularly thankful to Liulin Deng for the helpful discussion and design of the gas sensing setup and to Dr. Huanjun Chen for the XPS measurements.

Received: June 24, 2014
Revised: August 22, 2014
Published online: September 24, 2014

[1] M. P. Suh, H. J. Park, T. K. Prasad, D.-W. Lim, *Chem. Rev.* **2012**, *112*, 782.
[2] Y. Tachibana, L. Vayssieres, J. R. Durrant, *Nat. Photonics* **2012**, *6*, 511.
[3] H. Dotan, O. Kfir, E. Sharlin, O. Blank, M. Gross, I. Dumchin, G. Ankonina, A. Rothschild, *Nat. Mater.* **2013**, *12*, 158.
[4] H. Aki, Y. Taniguchi, I. Tamura, A. Kegasa, H. Hayakawa, Y. Ishikawa, S. Yamamoto, I. Sugimoto, *Int. J. Hydrog. Energy* **2012**, *37*, 1204.
[5] B.-G. Sun, D.-S. Zhang, F.-S. Liu, *Int. J. Hydrog. Energy* **2013**, *38*, 3778.
[6] X. Q. Zeng, M. L. Latimer, Z. L. Xiao, S. Panuganti, U. Welp, W. K. Kwok, T. Xu, *Nano Lett.* **2011**, *11*, 262.
[7] Z. J. Wang, Z. Y. Li, T. T. Jiang, X. R. Xu, C. Wang, *ACS Appl. Mater. Interfaces* **2013**, *5*, 2013.
[8] N. Liu, M. L. Tang, M. Hentschel, H. Giessen, A. P. Alivisatos, *Nat. Mater.* **2011**, *10*, 631.
[9] A. Tittl, P. Mai, R. Taubert, D. Dregely, N. Liu, H. Giessen, *Nano Lett.* **2011**, *11*, 4366.
[10] T. Shegai, P. Johansson, C. Langhammer, M. Käll, *Nano Lett.* **2012**, *12*, 2464.
[11] A. Tittl, X. H. Yin, H. Giessen, X.-D. Tian, Z.-Q. Tian, C. Kremers, D. N. Chigrin, N. Liu, *Nano Lett.* **2013**, *13*, 1816.
[12] M. L. Tang, N. Liu, J. A. Dionne, A. P. Alivisatos, *J. Am. Chem. Soc.* **2011**, *133*, 13220.
[13] C. Langhammer, E. M. Larsson, B. Kasemo, I. Zorić, *Nano Lett.* **2010**, *10*, 3529.
[14] L.-G. Ekedahl, M. Eriksson, I. Lundström, *Acc. Chem. Res.* **1998**, *31*, 249.
[15] F. Favier, E. C. Walter, M. P. Zach, T. Benter, R. M. Penner, *Science* **2001**, *293*, 2227.
[16] T. Hübert, L. Boon-Brett, G. Black, U. Banach, *Sens. Actuators B* **2011**, *157*, 329.
[17] G. Korotcenkov, S. D. Han, J. R. Stetter, *Chem. Rev.* **2009**, *109*, 1402.
[18] W. E. Vargas, I. Rojas, D. E. Azofeifa, N. Clark, *Thin Solid Films* **2006**, *496*, 189.
[19] K. M. Mayer, J. H. Hafner, *Chem. Rev.* **2011**, *111*, 3828.
[20] K. Saha, S. S. Agasti, C. Kim, X. N. Li, V. M. Rotello, *Chem. Rev.* **2012**, *112*, 2739.
[21] J. N. Anker, W. P. Hall, O. Lyandres, N. C. Shah, J. Zhao, R. P. Van Duyne, *Nat. Mater.* **2008**, *7*, 442.
[22] C.-Y. Chiu, M. H. Huang, *Angew. Chem. Int. Ed.* **2013**, *52*, 12709.
[23] C. Langhammer, I. Zorić, B. Kasemo, *Nano Lett.* **2007**, *10*, 3122.
[24] I. Zorić, E. M. Larsson, B. Kasemo, C. Langhammer, *Adv. Mater.* **2010**, *22*, 4628.

[25] C. Langhammer, E. M. Larsson, V. P. Zhdanov, I. Zorić, *J. Phys. Chem. C* **2012**, *116*, 21201.
[26] M. E. Nasir, W. Dickson, G. A. Wurtz, W. P. Wardley, A. V. Zayats, *Adv. Mater.* **2014**, *26*, 3532.
[27] T. Ming, H. J. Chen, R. B. Jiang, Q. Li, J. F. Wang, *J. Phys. Chem. Lett.* **2012**, *3*, 191.
[28] T. Ming, L. Zhao, H. J. Chen, K. C. Woo, J. F. Wang, H.-Q. Lin, *Nano Lett.* **2011**, *11*, 2296.
[29] H. J. Chen, L. Shao, Q. Li, J. F. Wang, *Chem. Soc. Rev.* **2013**, *42*, 2679.
[30] H. J. Chen, L. Shao, T. Ming, Z. H. Sun, C. M. Zhao, B. C. Yang, J. F. Wang, *Small* **2010**, *6*, 2272.
[31] R. B. Jiang, S. Cheng, L. Shao, Q. F. Ruan, J. W. Wang, *J. Phys. Chem. C* **2013**, *117*, 8909.
[32] M. D. Xiao, R. B. Jiang, F. Wang, C. H. Fang, J. F. Wang, J. C. Yu, *J. Mater. Chem. A* **2013**, *1*, 5790.
[33] F. Wang, C. H. Li, H. J. Chen, R. B. Jiang, L.-D. Sun, Q. Li, J. F. Wang, J. C. Yu, C.-H. Yan, *J. Am. Chem. Soc.* **2013**, *135*, 5588.
[34] N. Zhou, L. Polavarapu, N. Y. Gao, Y. L. Pan, P. Y. Yuan, Q. Wang, Q.-H. Xu, *Nanoscale* **2013**, *5*, 4236.
[35] S. Chang, Q. Li, X. D. Xiao, K. Y. Wong, T. Chen, *Energy Environ. Sci.* **2012**, *5*, 9444.
[36] X. Y. Xu, A. K. K. Kyaw, B. Peng, D. W. Zhao, T. K. S. Wong, Q. H. Xiong, X. W. Sun, A. J. Heeger, *Org. Electron.* **2013**, *14*, 2360.
[37] V. Janković, Y. M. Yang, J. B. You, L. T. Dou, Y. S. Liu, P. Cheung, J. P. Chang, Y. Yang, *ACS Nano* **2013**, *7*, 3815.
[38] H. J. Chen, X. S. Kou, Z. Yang, W. H. Ni, J. F. Wang, *Langmuir* **2008**, *24*, 5233.
[39] H. J. Chen, L. Shao, K. C. Woo, T. Ming, H.-Q. Lin, J. F. Wang, *J. Phys. Chem. C* **2009**, *113*, 17691.
[40] Q. Li, R. B. Jiang, T. Ming, C. H. Fang, J. F. Wang, *Nanoscale* **2012**, *4*, 7070.
[41] H. J. Chen, F. Wang, K. Li, K. C. Woo, J. F. Wang, Q. Li, L.-D. Sun, X. X. Zhang, H.-Q. Lin, C.-H. Yan, *ACS Nano* **2012**, *6*, 7162.
[42] Y. J. Xiang, X. C. Wu, D. F. Liu, X. Y. Jiang, W. G. Chu, Z. Y. Li, Y. Ma, W. Y. Zhou, S. S. Xie, *Nano Lett.* **2006**, *6*, 2290.
[43] F. Wang, L.-D. Sun, W. Feng, H. J. Chen, M. H. Yeung, J. F. Wang, C.-H. Yan, *Small* **2010**, *6*, 2566.
[44] H. W. Liao, J. H. Hafner, *Chem. Mater.* **2005**, *17*, 4636.
[45] C. J. Orendorff, C. J. Murphy, *J. Phys. Chem. B* **2006**, *110*, 3990.
[46] K. C. Woo, L. Shao, H. J. Chen, Y. Liang, J. F. Wang, H.-Q. Lin, *ACS Nano* **2011**, *5*, 5976.
[47] L. Shao, Q. F. Ruan, R. B. Jiang, J. F. Wang, *Small* **2014**, *10*, 802.
[48] R. B. Jiang, H. J. Chen, L. Shao, Q. Li, J. F. Wang, *Adv. Mater.* **2012**, *24*, OP200.
[49] E. H. Voogt, A. J. M. Mens, O. L. J. Gijzeman, J. W. Geus, *Surf. Sci.* **1996**, *350*, 21.
[50] P. O. Nilsson, M. S. Shivaraman, *J. Phys. C: Solid State Phys.* **1979**, *12*, 1423.
[51] L. M. Tian, E. Z. Chen, N. Gandra, A. Abbas, S. Singamaneni, *Langmuir* **2012**, *28*, 17435.
[52] N. N. Jiang, L. Shao, J. F. Wang, *Adv. Mater.* **2014**, *26*, 3282.
[53] H. J. Chen, T. Ming, S. R. Zhang, Z. Jin, B. C. Yang, J. F. Wang, *ACS Nano* **2011**, *5*, 4865.
[54] H. J. Chen, L. Shao, T. Ming, K. C. Woo, Y. C. Man, J. F. Wang, H.-Q. Lin, *ACS Nano* **2011**, *5*, 6754.
[55] L. Shao, C. H. Fang, H. J. Chen, Y. C. Man, J. F. Wang, H.-Q. Lin, *Nano Lett.* **2012**, *12*, 1424.
[56] F. Hao, P. Nordlander, *Chem. Phys. Lett.* **2007**, *446*, 115.